# Direct Observation of a Charge-Transfer State Preceding High-Yield Singlet Fission in Terrylenediimide Thin Films

Eric A. Margulies,[†] Jenna L. Logsdon,[†] Claire E. Miller, Lin Ma, Ethan Simonoff, Ryan M. Young,* George C. Schatz,* and Michael R. Wasielewski*

Department of Chemistry and Argonne-Northwestern Solar Energy Research Center, Northwestern University, 2145 Sheridan Road, Evanston, Illinois 60208-3113, United States

S Supporting Information

ABSTRACT: Singlet exciton fission (SF) in organic chromophore assemblies results in the conversion of one singlet exciton (S_1) into two triplet excitons (T_1), provided that the overall process is exoergic, i.e., $E(S_1) > 2E(T_1)$. We report on SF in thin polycrystalline films of two terrylene-3,4:11,12-bis(dicarboximide) (TDI) derivatives **1** and **2**, which crystallize into two distinct π-stacked structures. Femtosecond transient absorption spectroscopy (fsTA) reveals a charge-transfer state preceding a 190% T_1 yield in films of **1**, where the π-stacked TDI molecules are rotated by 23° along an axis perpendicular to their π systems. In contrast, when the TDI molecules are slip-stacked along their N—N axes in films of **2**, fsTA shows excimer formation, followed by a 50% T_1 yield.
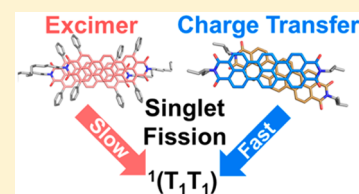
INTRODUCTION

Singlet exciton fission (SF) in organic chromophore assemblies results in the conversion of one singlet exciton (S_1) into two triplet excitons (T_1), provided that the overall process is exoergic, i.e., $E(S_1) > 2E(T_1)$. Recent interest in elucidating the SF mechanism has grown rapidly because of its potential for increasing the maximum efficiency of photovoltaics from the 33% Shockley−Queisser limit for single-junction devices to nearly 45%.[1−3] Given this advantage, SF has been investigated in a number of polyacenes,[4−12] polyenes,[13−15] and other chromophores.[16−20] SF can occur by two general mechanisms: one that directly couples the photogenerated initial $^1(S_1S_0)$ state to a multi-exciton $^1(T_1T_1)$ state by a two-electron process, and another that proceeds through a charge-transfer (CT) state by two consecutive one-electron processes.[3] The participation of CT states in the SF mechanism is suggested by the observed SF rate dependence on solvent polarity in covalent diphenylisobenzofuran[21] and pentacene dimers,[22−24] as well as the direct observation of the symmetry-breaking ion pair formation in terrylene-3,4:11,12-bis(dicarboximide) (TDI) dimers.[25] A notable exception is a covalent pentacene dimer linked at the pentacene 2-position that shows no such solvent polarity dependence.[26] However, the various states involved in SF have recently been shown to engage in interactions that are more complex.[4,10,27−30]

Photoexcitation of a chromophore that is electronically coupled to a second nearby chromophore may create an electronic superposition state involving $^1(S_1S_0)$, a virtual CT state, and $^1(T_1T_1)$.[28] Electronic dephasing of this superposition state typically should occur on a sub-picosecond time scale leaving the spin-coherent $^1(T_1T_1)$ state, which is usually referred to as a correlated triplet pair state. Spin dephasing is a much slower process, typically on the order of nanoseconds,[10] so that spin dephasing in $^1(T_1T_1)$ may occur on a time scale

comparable to the spatial separation of the triplet states, resulting in two independent triplet states.[28] Here, we investigate SF in thin polycrystalline films of two TDI derivatives **1** and **2**, which crystallize into two distinct π-stacked structures. In the structure of **1** (Figure 1) the TDI molecules are rotated along an axis perpendicular to their π systems by 23°, while in **2**, a modest amount of slip-stacking along the N—N axis direction of the TDI molecules occurs. Vapor-deposited thin films of **1** and **2** preserve the essential single-crystal structural features. Femtosecond transient absorption (fsTA) spectroscopy of a film of **1** shows that the initial state produced following photon absorption has substantial CT character leading to near-quantitative SF, while that of **2** shows primarily excimer formation and a modest 50% SF yield.

MATERIALS AND METHODS

TDI chromophores **1** and **2** were synthesized as described in the Supporting Information by two methods described previously.[31,32]

Structural Characterization. Single crystals of **1** and **2** were grown from boiling nitrobenzene that was slowly cooled to room temperature over 12 h. The crystals were mounted on MiTeGen MicroLoops with Paratone oil and data were collected at 100 K on a Bruker Kappa APEX II CCD diffractometer equipped with a CuKα IμS microfocus source with Quazar Optics. All data was absorption corrected using SADABS. The structures were solved using SHELXS and refined using SHELXT. Structures have been deposited in the Cambridge Structural Database (CCDC Nos. 1491228 and 1491229), and the CIF files for **1** and **2** are available as Supporting Information.

Film Fabrication and Characterization. Prior to film fabrication, **1** and **2** were further purified by gradient sublimation (200−300 °C, 10^{-6} Torr). Thin-film samples were vapor-deposited using an
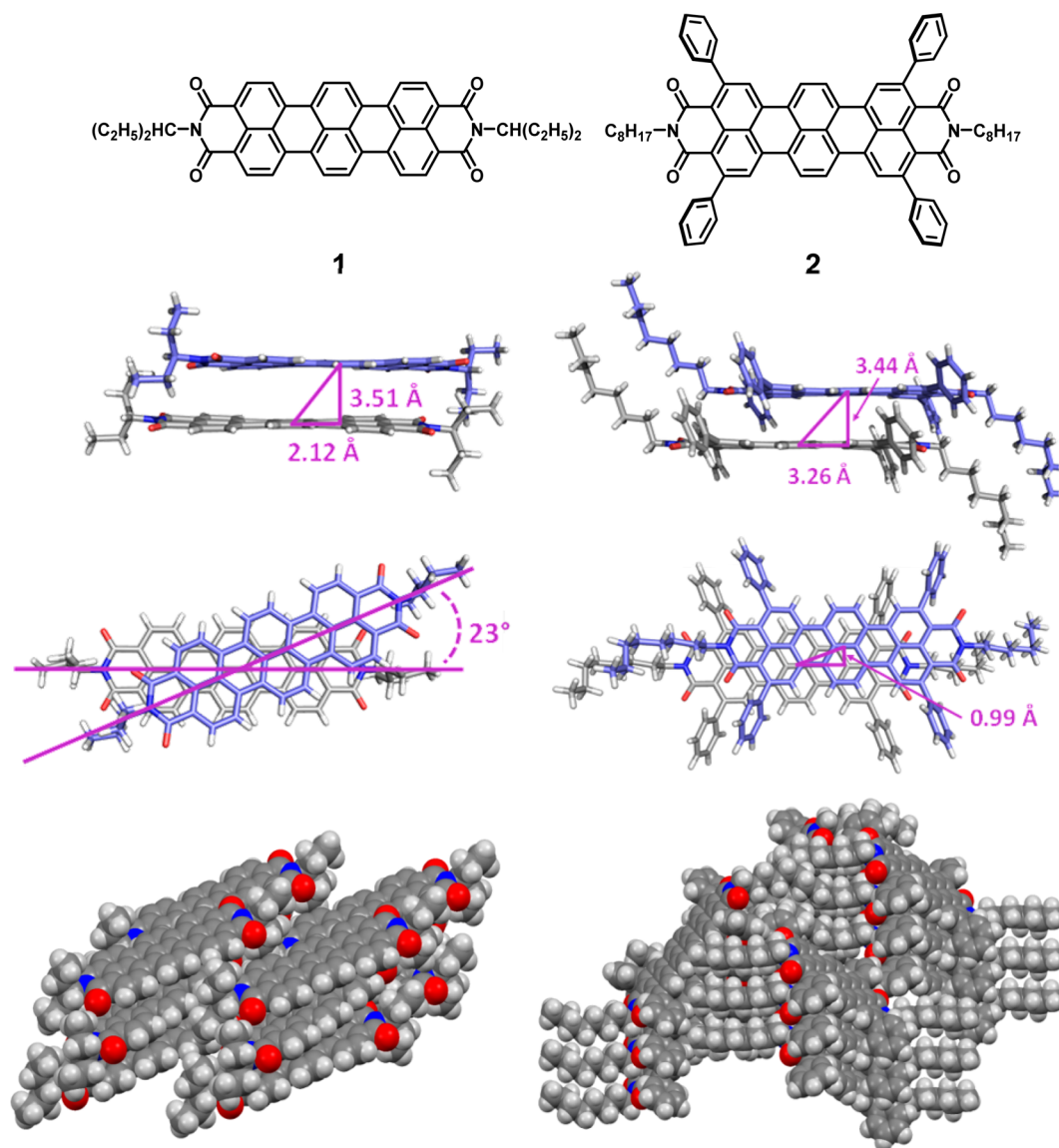
Figure 1. Chemical and single-crystal X-ray diffraction structures of **1** and **2**.

Angstrom Engineering Covap II physical vapor deposition system. Three batches of films of **1** and **2** were prepared. Batches A and B of films of **1** and **2** were evaporated onto room temperature (22 °C) ArrayIt Super Clean 2 glass slide substrates (25.4 mm diameter × 1 mm thickness) at a rate of 0.5 Å/s, while batch C was evaporated under the same conditions on a polished sapphire substrate ((25.4 mm diameter × 1 mm thickness, Ted Pella, Inc. Redding, CA). Crystalline samples were prepared by solvent vapor annealing (SVA) the films with dichloromethane (DCM) vapor in a sealed vial for 24 h at which point the absorption spectrum had ceased evolving.

Film thicknesses were measured by surface profilometry with a Veeco Dektak 150 surface profiler equipped with a 25 μm diameter stylus. Film thicknesses for batch A are 78 nm for **1** and 38 nm for **2**, which resulted in an optical density of 0.24 at 607 nm and 0.13 at 612 nm, respectively, while those of batches B and C are 65 nm for **1** and 35 nm for **2** with proportional optical densities. Grazing incidence X-ray diffraction measurements were performed using a Rigaku SmartLab diffraction system with an incident angle of 0.2°. The resulting diffractograms were manually background subtracted using Rigaku PDXL software.

Steady-State Optical Characterization. Solution phase absorption spectra were recorded on a Shimadzu 1800 spectrophotometer. Film absorption spectra were recorded on a PerkinElmer LAMBDA

1050 UV/vis/NIR spectrophotometer equipped with an integrating sphere (150 mm) and the scatter-free absorption spectra were calculated by the Beer−Lambert law and the sum of the reflected and transmitted light. Emission spectra were recorded using a Horiba Nanolog fluorimeter with a perpendicular arrangement of the excitation source and detector. The spectra were corrected for the monochromator wavelength dependence and CCD-detector spectral response functions provided by the manufacturer. Unusually long integration times of 15 and 10 s (limited by detector dark noise) were needed to record spectra of films of **1** and **2**, respectively. Attempts to measure a fluorescence quantum yield for these films yields only an estimate that both yields are <0.01.

Transient Absorption Spectroscopy. Visible and near-infrared (NIR) femtosecond transient absorption (fsTA) as well as nanosecond transient absorption (nsTA) measurements were all performed using previously described instruments.[12,33] The data were modeled using global analysis of the data with a specific kinetic model using a lab-written MATLAB (The Mathworks, Inc.) program.[34]

We globally fit the data set to a specified kinetic model and use the resultant populations to deconvolute the data set and reconstruct species-associated spectra. The MATLAB program solves the differential equations numerically using the Runge−Kutta algorithm, then convolutes the solutions with a Gaussian instrument response
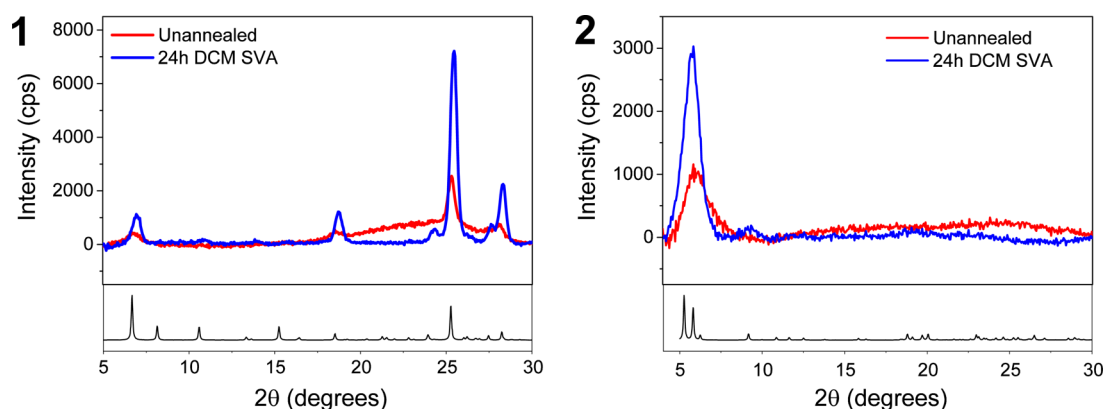
Figure 2. GIXRD diffractograms and simulated powder patterns (black) of **1** and **2** films in Batch A.

function before employing an iterative least-squares fitting to find the parameters which result in matches to the kinetic data. Once the kinetic fit parameters are established, they are fed directly into the differential equations, which are solved for the populations of the states in the model, i.e., $A(t)$, $B(t)$, and $C(t)$. Finally, the raw data matrix (with all the raw data) is deconvoluted with these populations as functions of time to produce the spectra associated with each species.

The data for **1** were fit to the following nonlinear model:

$$\frac{d[S_1^{(1)}]}{dt} = -k_{SF1}[S_1^{(1)}] - \frac{k_{SSA}}{2}[S_1^{(1)}]^2$$

$$\frac{d[S_1^{(2)}]}{dt} = -k_{SF2}[S_1^{(2)}]$$

$$\frac{d[T_1]}{dt} = 2k_{SF1}[S_1^{(1)}] + 2k_{SF2}[S_1^{(2)}] - \frac{k_{TTA}}{2}[T_1]^2 \qquad (1)$$

where k_{SSA} is the singlet–singlet annihilation (SSA) rate constant, k_{TTA} is the triplet–triplet annihilation rate constant, and k_{SF1} and k_{SF2} are the two SF rate constants, respectively. The observed biexponential decay of the singlet state is modeled as two independent populations representing the dominant populations in the heterogeneous film. The initial populations of the two singlet excited states were equally weighted, i.e., $[S_1^{(1)}](0) = [S_1^{(2)}](0) = 0.5$. This initial condition ensures the total triplet yield in the model is ≤ 2. In reality, the distribution of structures leading to the two representative populations is not the same; however, deviations from these initial conditions are encoded into the relative intensities of the species-associated spectra. SSA is assumed to only affect the population experiencing the fastest SF decay, where the two processes are competitive. The term that accounts for singlet–singlet annihilation[19] was not needed to model the 10^{17} cm^{-3} excitation density data.

Following instrument-limited formation of the TDI excimer for **2**, we model the excimer relaxation process and SF proceeding from the relaxed excimer with a sequential kinetic model, along with a strong coherence artifact attributed to a (parallel) nonresonant response of the sample to the strong laser field during pump–probe overlap:

$$\frac{d[Ex^*]}{dt} = -k_{RLX}[Ex^*]$$

$$\frac{d[Ex]}{dt} = k_{RLX}[Ex^*] - k_{Ex}[Ex] - k_{SF}[Ex]$$

$$\frac{d[T_1]}{dt} = 2k_{SF}[Ex] - \frac{k_{TTA}}{2}[T_1]^2 \qquad (2)$$

where k_{RLX} is the excimer relaxation rate constant observed in the initial excimer state, and k_{Ex} is the excimer decay to ground-state rate constant. The ratio of the SF rate constant (k_{SF}) and the excimer decay rate constant (k_{Ex}) was fixed, based on the triplet yield ϕ_T (~50% for **2**) obtained from the nanosecond transient absorption (nsTA) data:

$$k_{Ex} = k_{SF}\left(\frac{2}{\Phi_T} - 1\right) \approx 3k_{SF} \qquad (3)$$

Electronic Coupling Calculations. The electronic coupling between two TDI molecules comprising a dimer was calculated using the fragment orbital approach as implemented in the Amsterdam density functional (ADF) package.[35] Fragments were created by optimizing the geometry of a TDI monomer, using a double-ζ (DZ) basis set and B3LYP functional, and then expanding the basis set to triple-ζ double polarization (TZ2P). The optimized geometry of one molecule was then shifted and/or rotated to the desired slip-stacking distance and rotation angle with respect to the second molecule. The electronic coupling for each transition was calculated using the equation,[36]

$$V_{fi} = \frac{\left(J_{fi} - \frac{S_{fi}(e_i + e_f)}{2}\right)}{1 - S_{fi}^2} \qquad (4)$$

where J_{fi} is the charge transfer integral, S_{fi} is the overlap integral, and e is the site energy of the initial (i) or final (f) state, respectively.

RESULTS AND DISCUSSION

Structural Characterization. Compound **1** crystallizes in the $C2/c$ space group with one half molecule in the asymmetric unit. The TDI core exhibits a slight core twist of 4.8° between adjacent naphthalene subunits. Owing to a strong association of their π-planes, the TDI molecules form a π-stacked assembly with 3.51 Å π–π distances as shown in Figure 1. All π-stacks are found to be oriented in the same direction, roughly along the crystal c-axis. Additionally, the steric bulk of the 3-pentyl tail prohibits a more cofacial interaction, which is common in rylene aggregates,[37] and induces a longitudinal slip distance of 2.12 Å as well as a yaw angle (φ) of 23° between the long axes of adjacent TDIs. Compound **2** also crystallizes in the $C2/c$ space group, and the TDI core is again slightly twisted, with an angle of 3.9° between adjacent naphthalene subunits. The phenyl substituents of **2** induce a slip-stacked motif as shown in Figure 1. Unlike **1**, the π-stacks of **2** are found to be oriented in different directions, with adjacent π-stacks in a herringbone configuration to one another (space-filling structures, Figure 1). Even though the influence of the four phenyl groups in **2** results in a slip-stacked crystal structure with a longitudinal displacement of 3.26 Å, similar to that we reported for the corresponding 2,5,8,11-tetraphenylperylene-(3,4:9,10)-bis-(dicarboximide) (PDI),[18] the larger π-surface of TDI relative to that of the PDI derivative results in greater π overlap in TDI. This increased electronic interaction often results in ultrafast
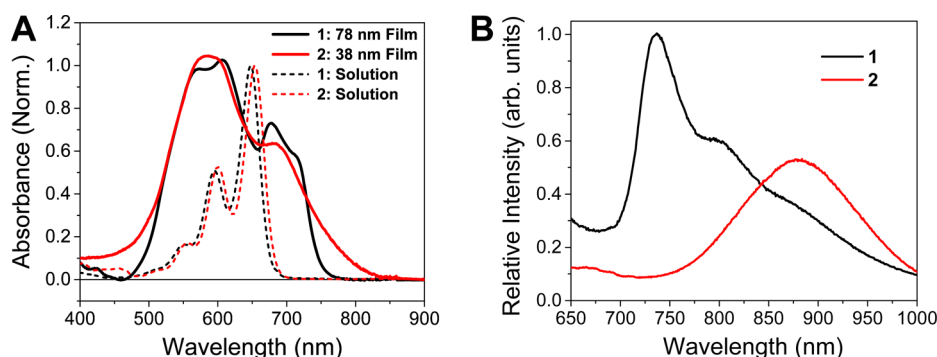
Figure 3. (A) Normalized UV−vis absorption spectra of **1** and **2** in dichloromethane solution and in vapor-deposited thin films subsequently solvent vapor-annealed with dichloromethane for 24 h. (B) Fluorescence spectra of vapor-deposited, solvent vapor-annealed thin films of **1** and **2** from batch A.

rates of excimer formation that can effectively compete with SF rates (see below).

Thin films samples of **1** and **2** were prepared by vapor deposition in high vacuum followed by solvent vapor annealing with dichloromethane for 24 h. Grazing incidence X-ray diffraction (GIXRD) measurements were performed to determine the extent and nature of aggregation in the thin film samples as well as draw comparisons with the single crystal structures. Diffractograms of the annealed films of **1** and **2** were collected and compared with simulated powder patterns. The resulting diffractograms of **1** and **2** (Figure 2) are in good agreement with the simulated powder patterns, thus implying that the intermolecular interactions observed in the film are similar to those in the respective single crystal structures. The diffraction pattern of **2** contains relatively fewer peaks compared to **1** with a predominant peak corresponding to a reflection from the (200) plane, implying a highly textured film with the TDI molecules oriented edge-on relative to the substrate plane.

Steady-State Spectroscopy. TDI is a highly stable and strongly absorbing ($\lambda_{650} = 93000$ M^{-1} cm^{-1}, $E(S_1) = 1.87$ eV)[38] chromophore with a triplet-state energy ($E(T_1) \leq 0.77$ eV) low enough to allow SF.[25] The UV−vis absorption spectra of **1** and **2** in dichloromethane shown in Figure 3A are very similar and have absorption maxima at 648 and 654 nm, respectively, which indicates that that the addition of 2,5,10,13-tetraphenyl substituents has a negligible effect on the TDI $S_1 \leftarrow S_0$ energy. UV−vis absorption spectra for thin films of **1** and **2** are also shown in Figure 3A. The red-shifted low-energy absorption onset in the spectra of **1** and **2** is clear evidence of significant inter-chromophore electronic coupling typical of strongly π-associated rylene chromophores.[18,39−43] H-type excitonic coupling,[44] which is expected due to the small slip angles observed in the crystal structures, leads to a strong enhancement of the blue region of the absorption spectrum. Interestingly, despite a greater longitudinal slip distance in **2**, the absorption spectrum of **2** appears similar to that of **1**. This results from the $\varphi = 23°$ TDI−TDI rotation in the crystal structure of **1**, which reduces its inter-chromophore electronic coupling. Fluorescence spectra of the films (Figure 3B) were recorded after extensive averaging using a CCD detector (see Materials and Methods). The fluorescence quantum yields of the films were both <0.01 precluding accurate measurement of their fluorescence lifetimes using our femtosecond fluorescence upconversion system. The energy of the onset of the highest energy emission band in the films shows that $E(S_1) = 1.77$ eV

for **1**, while $E(S_1) = 1.66$ eV for **2**. Since the triplet energy of TDI is <0.77 eV, $E(S_1) > 2 E(T_1)$ for both **1** and **2** in the solid state.

Femtosecond Transient Spectroscopy. The excited-state dynamics of **1** and **2** in solution were investigated by fsTA spectroscopy (Figure S1). After photoexcitation at 600 nm, the transient spectrum of **1** exhibits ground-state bleach (GSB) minima near 597 and 652 nm, a stimulated emission (SE) feature at 738 nm, and three sharp $S_n \leftarrow S_1$ absorptions at 870, 1070, and 1234 nm. These features all decay concomitantly in τ = 2.5 ± 0.2 ns. The transient spectra of **2** are very similar, with some of the features being somewhat red-shifted relative to **1** because of a slight increase in conjugation length provided by the four phenyl groups. The GSB features occur at 600 and 660 nm, while the SE feature occurs at 741 nm and the near-infrared (NIR) bands absorb at 890, 1075, and 1237 nm. These bands decay in concert in τ = 2.7 ± 0.1 ns. Both **1** and **2** show no evidence of triplet-state formation in solution at the ~10^{-4} M concentrations used.

FsTA spectroscopy was used to characterize the excited-state dynamics of batch A thin films of **1** and **2** in the 475−800 nm and 850−1600 nm regions using 600 nm, 100 fs laser pulses at 1 kHz repetition rate and an excitation density = 1.0 × 10^{18} cm^{-3} (Figure 4). A second set of fsTA data was acquired on batch A films in the 475−800 nm region using 600 nm, 100 fs pulses at a 100 kHz repetition rate and an excitation density = 1.0 × 10^{17} cm^{-3} (Figures S2 and S4, a NIR detector is not currently available for the 100 kHz spectrometer). Additional low-fluence data sets were acquired on films of **1** and **2** on glass (batch B, Figures S6 and S8) and on sapphire (batch C, Figures S10 and S12), and will be discussed below.

In the 475−800 nm region, the transient spectra of **1** are consistent with S_1 ESA overlapped with the TDI GSB. In agreement with the ground-state absorption spectrum, GSB minima are observed at 565, 615, and 725 nm. A broad ESA is superimposed on the GSB, yielding positive features at 665 nm and 750−800 nm. The 850−1600 nm spectra of **1** show $S_n \leftarrow S_1$ absorption features similar to, but slightly blue-shifted relative to those in solution with maxima at 850, 1054, and 1204 nm. In addition, new maxima at 929 and 1298 nm are observed, which are very similar to two of the three NIR bands observed for TDI$^{-•}$.[25] The third TDI$^{-•}$ NIR band may be convolved with the broad band at 1054 nm.[25] These bands are absent in the solution fsTA data, and their presence in films of **1** indicates that the TDI CT state (TDI$^{+•}$−TDI$^{-•}$) is formed. Figure 5 shows an overlay of the normalized transient absorption spectra
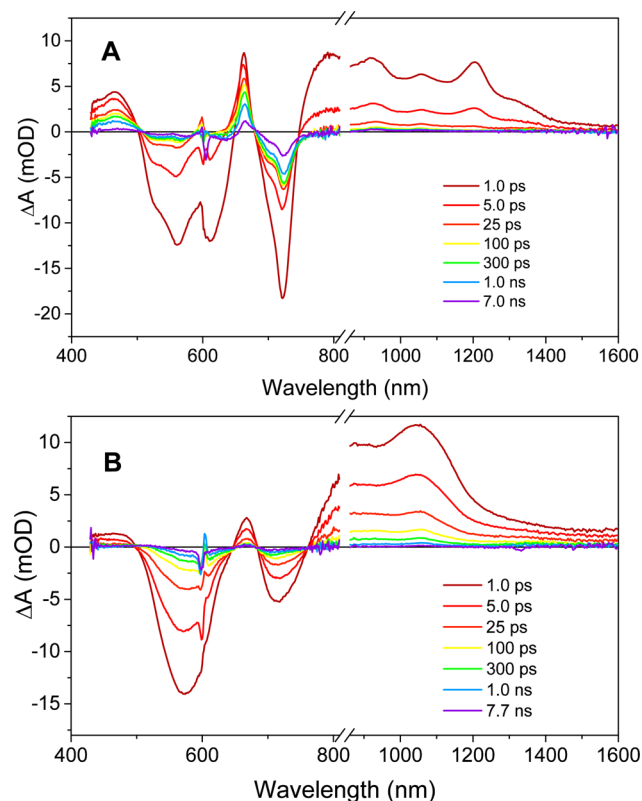
Figure 4. Transient absorption spectra of batch A films: (A) 78 nm thick film of **1** on glass and (B) 38 nm film of **2** on glass following a 600 nm, 100 fs laser pulse.
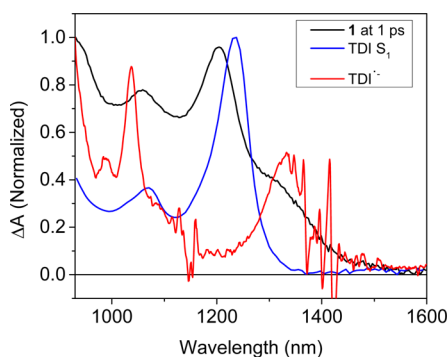
Figure 5. Overlay of the normalized transient absorption spectra of the TDI S_1 state, the spectrum of the film of **1** at 1 ps following excitation, and the spectrum of TDI$^{-\bullet}$ generated by cobaltocene reduction (ref 25).

of the TDI S_1 state, the spectrum of the film of **1** at 1 ps following excitation, and the spectrum of TDI$^{-\bullet}$ generated by cobaltocene reduction.[25] The corresponding 760 nm TDI$^{+\bullet}$ band[25] is most likely strongly overlapped with the $S_n \leftarrow S_1$ features at 750–800 nm. The CT energy estimated from the sum of the one electron redox potentials for TDI[47] is 1.75 eV, which is close to the estimated 1.77 eV energy of $^1{}^*$TDI in the film of **1**.

Both the high and low excitation density data for films of **1** on glass substrates Figures 4A and S2, respectively, were subjected to global fitting and analysis to yield the kinetic fits, species-associated spectra, and population kinetics shown in Figures 6 and S3, respectively, using the procedures and kinetic model (eq 1) outlined in the Materials and Methods. The

formation of the CT state from the $^1(S_1S_0)$ state cannot be resolved with 100 fs temporal resolution, and it is likely that the observed species-associated spectrum is that of a $^1(S_1S_0)$−CT mixed state. The decay of this spectrum results in the formation of the TDI T_1 transient spectrum[25] that persists beyond the 8 ns fsTA apparatus time window. The strong overlap of the GSB and $T_n \leftarrow T_1$ spectrum results in substantial cancellation of the overall $T_n \leftarrow T_1$ ΔA observed. The global fits to the higher excitation density data show that SF proceeds with two rate constants, $k_{SF1} = (2.7 \pm 0.2 \text{ ps})^{-1}$ and $k_{SF2} = (28 \pm 1 \text{ ps})^{-1}$ (Figure 6), which may be due to structural disorder in the film giving rise to a population of singlet excitons that must diffuse to sites at which SF is more favorable as has been suggested for tetracene derivatives.[7,12] A similar analysis of the 10^{17} cm^{-3} excitation density data shows similar SF kinetics with $k_{SF1} = (3.0 \pm 0.2 \text{ ps})^{-1}$ and $k_{SF2} = (31 \pm 1 \text{ ps})^{-1}$ (Figure S3). The species-associated spectra and species population kinetics are also very similar for the high and low excitation density data in the visible spectral region.

Both the high and low excitation density fsTA spectra of **2** on glass substrates (Figures 4B and S4) are marked by a more blue-shifted GSB than **1**, due to the *H*-type absorption spectrum of **2**. A comparison of the excimer-like spectrum obtained from the thin film of **2** with that of a covalent, cofacial TDI dimer[25] shows that they are very similar (Figure 7). We fit the fsTA data to the kinetic model (eq 2) given in the Materials and Methods, in which the excimer-like spectrum (Ex*) appears within the instrument response and the initial 1055 nm NIR ESA band subsequently undergoes a 5 nm blue shift with $k_{RLX} = (1.5 \pm 0.2 \text{ ps})^{-1}$, which we assign to structural relaxation of Ex* to form Ex similar to what is observed for TDI and PDI dimers.[25,48] Ex decays to ground state in competition with SF from Ex with $k_{SF} = (46 \pm 1 \text{ ps})^{-1}$ (Figure 8). Once again, comparing the data obtained at a 10^{18} cm^{-3} excitation density with those measured at 10^{17} cm^{-3} (Figures 8 and S5), the relaxation rate constant of the excimer state, $k_{RLX} = (1.2 \pm 0.6 \text{ ps})^{-1}$, and the SF rate constant $k_{SF} = (50 \pm 2 \text{ ps})^{-1}$ are essentially unchanged. The slower SF rate of **2** relative to **1** may result from the fact that the energy gap between the Ex state and the TDI triplet state is less favorable in **2**. The formation of an initial excimer-like state is consistent with the larger degree of TDI π-overlap in films of **2** relative to that in films of the corresponding PDI derivative, which undergoes high-yield SF.[18]

At excitation densities of 10^{18} cm^{-3} used to obtain the data on films of **2** in the UV−vis and NIR region, our data are consistent with a competition between singlet−singlet annihilation and excimer formation on a time scale comparable to our instrument response function, so that we cannot resolve these two events. However, using excitation densities of 10^{17} cm^{-3} eliminates singlet−singlet annihilation, while still resulting in excimer formation at times comparable to the instrument response function. The transient absorption spectra are broad and tail out past 1300 nm, which may again indicate a CT contribution to Ex* and Ex. However, in this case the Ex energy in the film of **2** is about 1.66 eV and is lower than the estimated 1.75 eV energy of the CT state, so that mixing of the CT state with the initial singlet excimer state should be weaker.

Possible Excitation Density and Thermal Laser Effects on the Data. The discussion above shows that data obtained at excitation densities of 10^{17} and 10^{18} cm^{-3} for molecules **1** and **2** on glass substrates are very similar as long as singlet− singlet annihilation at the higher excitation density is properly taken into account. As a further check, additional fsTA data
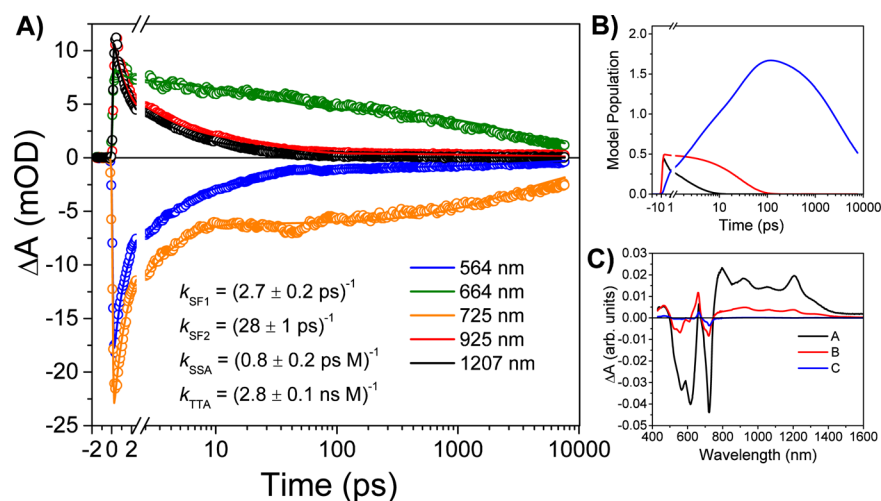
Figure 6. Analysis of the raw data for **1** shown in Figure 4A as described in the text. (A) Kinetics fits to the raw data at the indicated wavelengths. (B) Model population kinetics. (C) Species-associated spectra.
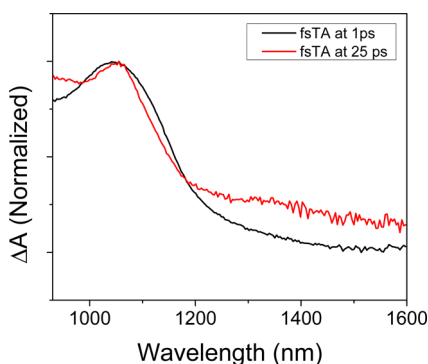

Figure 7. Comparison of the excimer-like spectra obtained from the thin film of **2** with that of a covalent, cofacial TDI dimer (ref 25).

were obtained at intermediate excitation densities for the same films (Figure S14). In all cases, the transient spectra and kinetics at each excitation density are essentially the same within the signal-to-noise of the data.

It was recently pointed out that laser heating of thin film samples can result in significant distortions of their transient absorption spectra and kinetics.[45] To check our data for potential heating problems, we prepared two new batches of films of **1** and **2**. Batch B is another set of films on glass substrates, while batch C uses sapphire substrates. The high thermal conductivity of sapphire relative to glass[45] makes it possible to assess whether heating effects distort the transient kinetics. Figures S6 and S10 show the raw fsTA data sets for a 64 nm film of **1** on glass and sapphire, respectively, while Figures S7 and S11 present the kinetic fits to the data along with the species associated spectra and species population kinetics using the model in eq 1. There are only small differences between the data, and the fits show that $k_{SF1} = (6.7 \pm 0.4 \text{ ps})^{-1}$ and $k_{SF2} = (72 \pm 3 \text{ ps})^{-1}$ on glass while $k_{SF1} = (6.0 \pm 0.4 \text{ ps})^{-1}$ and $k_{SF2} = (97 \pm 5 \text{ ps})^{-1}$ on sapphire. The kinetics at the 664 nm maximum of the triplet are given in Figure S15, once again showing little variation outside the signal-to-noise of the data.

A comparable data set was acquired on films of **2** on glass and sapphire. Figures S8 and S12 show the raw fsTA data sets for a 35 nm film of **2** on glass and sapphire, respectively, while Figures S9 and S13 present the kinetic fits to the data along
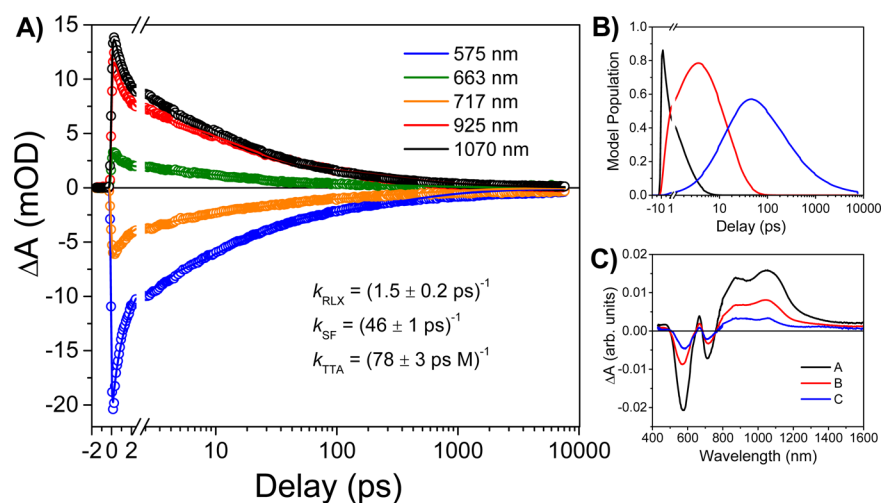
Figure 8. Analysis of the raw data for **2** shown in Figure 4B as described in the text. (A) Kinetics fits to the raw data at the indicated wavelengths. (B) Model population kinetics. (C) Species-associated spectra.
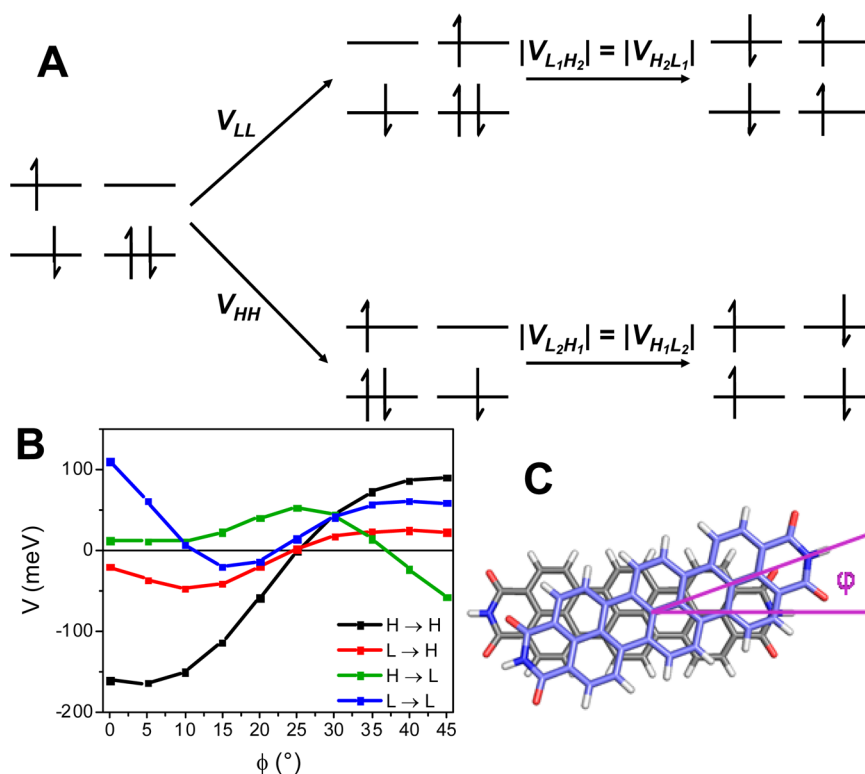
Figure 9. (A) Schematic of the CT-mediated SF mechanism showing the relevant one-electron couplings. (B) Plot of the four calculated couplings as a function of (C) the definition of TDI yaw angle, φ.

with the species associated spectra and species population kinetics using the model in eq 2. The fits show that $k_{RLX} = (1.4 \pm 0.1 \text{ ps})^{-1}$ and $k_{SF} = (110 \pm 10 \text{ ps})^{-1}$ on glass, while $k_{RLX} = (3.8 \pm 0.6 \text{ ps})^{-1}$ and $k_{SF} = (160 \pm 10 \text{ ps})^{-1}$ on sapphire. The kinetics at the 664 nm maximum of the triplet are given in Figure S16. Here too, despite the somewhat lower signal-to-noise of the data, there are no dramatic differences in the kinetics of **2** on glass and sapphire.

Finally, we used the method of Rao et al. to estimate an upper limit of heating from photoexcitation,[45] assuming heat capacities similar to those measured for a perylene crystal (274.9 J/mol K).[46] We calculate that the temperature change is $\Delta T = 0.09$ K for TDI at the 10^{17} cm^{-3} excitation densities used here.

Triplet Yields. The triplet yields in films of **1** and **2** were determined using nsTA spectroscopy (Figure S17). These spectra closely resemble the transient spectra observed at long time delays (>100 ps) in the fsTA experiments, except near 600 nm in the fsTA spectra, where pump scatter corrections distort the spectra somewhat. Again we find the long-lived triplet signal in **1** to be significantly larger than **2**. The singlet depletion method,[49] which has been demonstrated to be effective in obtaining SF yields in pentacene dimers,[50] diketopyrrolopyr-roles,[20] and rylenes,[18,19] was used to obtain the triplet yields in thin films of **1** and **2** (Figures S18 and S19). The results of this analysis show that the thin film of **1** has a 190% triplet yield, while that of **2** has a much lower 50% triplet yield. It should be pointed out that it is difficult to assign triplet yields that are <100% unequivocally to SF. While spin orbit-induced intersystem crossing in monomeric TDI results in a <1% triplet yield, given the favorable SF energetics of TDI, we will assume here that the enhanced triplet results from SF and not from enhanced intersystem crossing from the excimer state.

The analysis of the fsTA data using 10^{18} cm^{-3} excitation density (Figure 6B) shows that the maximum triplet-state population of **1** is 168%, while that using 10^{17} cm^{-3} excitation density (Figure S3B) gives a 190% maximum triplet population, which is in agreement with the annihilation-free nsTA data, and indicates that 11% of the initially formed singlet states of **1** decay by SSA in the higher fluence fsTA experiments. For **2**, the excimer state does not undergo SSA, so that both the high and low laser fluence fsTA data (Figures 8B and S5B) give a 55% maximum triplet population, which agrees well with the nsTA measurements on **2**. Thus, the triplet yields are self-consistent.

Electronic Coupling Matrix Elements. To evaluate the effect that intermolecular geometry has on SF, the one electron coupling matrix elements for the pairwise HOMO–LUMO interactions (V_{HH}, V_{LL}, V_{HL}, and V_{LH}) were calculated. Previous investigations of these interactions in a coupled chromophore pair have yielded structural information about the CT-mediated SF mechanism and have shown good agreement with experimental results.[36,51−53] In the two-step CT-mediated SF mechanism, symmetric coupling of adjacent HOMO–HOMO and LUMO–LUMO pairs (V_{HH} and V_{LL}) facilitates the first step of CT-state formation (Figure 9). The HOMO–LUMO and LUMO–HOMO couplings (V_{HL} and V_{LH}) are then responsible for the formation of the $^1(T_1T_1)$ pair from the CT state, and are particularly important to the overall efficiency of the CT-mediated process when the CT state is directly formed from S_1.[36] To study this, we calculated these one-electron couplings for a TDI dimer as a function of the φ angle, which was observed to be 23° in the crystal structure of **1**. We find the magnitude of the V_{HL} and V_{LH} couplings to be greatly dependent on this angle. Although one might expect the V_{HL} and V_{LH} coupling to be equal in magnitude and antisymmetric to each other, the loss of molecular symmetry in the

arrangement of the dimer used for these calculations results in differing values depending on the localization of the HOMO and LUMO. However, we expect both of these calculated coupling values can contribute to the overall HOMO−LUMO coupling in the symmetric crystal structure.

We plot the one-electron couplings as a function of the φ angle (Figure 9) using a slip-stacking distance of 2.12 Å, which is extracted from the crystal structure of **1**, and a $\pi-\pi$ interplanar distance of 3.5 Å. The results of this calculation show a maximum of 53 meV in the HOMO−LUMO coupling at $\varphi = 25°$, similar to the 23° angle exhibited in the crystal structure of **1**. Assuming that this coupling is essential to CT-mediated SF, this suggests the importance of the φ angle in promoting SF in TDI-based materials. These results directly support the observation that SF is efficient in **1** but not in **2** because the intermolecular electronic coupling is more favorable in the yawed ($\varphi \neq 0$) geometry of **1**. This conclusion bears resemblance to the previous finding that a slip-stacked arrangement leads to a more favorable HOMO−LUMO interaction for SF,[3] and moreover, expands this view to include a broader scope of intermolecular geometries.

CONCLUSIONS

Our previous work on covalent TDI dimers showed that formation of a charge-transfer state whose energy is below those of $^1(S_1S_0)$ and $^1(T_1T_1)$ results in the CT state serving as a trap state that competes effectively with singlet fission. In the case of thin films of **1**, the appearance of transient absorption bands characteristic of the TDI radical anion strongly suggests that the CT state is nearly isoenergetic with $^1(S_1S_0)$ and $^1(T_1T_1)$, resulting in nearly quantitative SF. Given the instrument response limited formation time of the CT state in films of **1**, we cannot rule out the possibility that the CT state is strongly mixed with $^1(S_1S_0)$, and possibly with $^1(T_1T_1)$ as well. Given the clear differentiation between the sharp TDI $S_n{\leftarrow}S_1$ and CT-state absorptions in the NIR spectral region, studies of SF in TDI derivatives afford the opportunity to explore the overall SF mechanism in more detail. In addition, the high SF yield observed in **1** highlights the broader scope of inter-chromophore geometries that can lead to favorable electronic couplings and CT-state involvement in SF.

ASSOCIATED CONTENT

Ⓢ Supporting Information

The Supporting Information is available free of charge on the ACS Publications website at DOI: 10.1021/jacs.6b07721.

> Details including synthesis, NMR and MS characterization, X-ray structural data, and fsTA and nsTA data, including Figures S1−S19 and Tables S1−S3 (PDF)
> X-ray crystallographic data for **1** (CIF)
> X-ray crystallographic data for **2** (CIF)

AUTHOR INFORMATION

Corresponding Authors
*ryan.young@northwestern.edu
*g-schatz@northwestern.edu
*m-wasielewski@northwestern.edu

ORCID Ⓞ
Michael R. Wasielewski: 0000-0003-2920-5440

Author Contributions
†E.A.M. and J.L.L. contributed equally to this work.

Notes
The authors declare no competing financial interest.

REFERENCES
(1) Shockley, W.; Queisser, H. J. *J. Appl. Phys.* **1961**, *32*, 510.
(2) Hanna, M. C.; Nozik, A. J. *J. Appl. Phys.* **2006**, *100*, 074510/1.
(3) Smith, M. B.; Michl, J. *Chem. Rev.* **2010**, *110*, 6891.
(4) Chan, W.-L.; Ligges, M.; Jailaubekov, A.; Kaake, L.; Miaja-Avila, L.; Zhu, X.-Y. *Science* **2011**, *334*, 1541.
(5) Ramanan, C.; Smeigh, A. L.; Anthony, J. E.; Marks, T. J.; Wasielewski, M. R. *J. Am. Chem. Soc.* **2012**, *134*, 386.
(6) Chan, W.-L.; Ligges, M.; Zhu, X. Y. *Nat. Chem.* **2012**, *4*, 840.
(7) Roberts, S. T.; McAnally, R. E.; Mastron, J. N.; Webber, D. H.; Whited, M. T.; Brutchey, R. L.; Thompson, M. E.; Bradforth, S. E. *J. Am. Chem. Soc.* **2012**, *134*, 6388.
(8) Walker, B. J.; Musser, A. J.; Beljonne, D.; Friend, R. H. *Nat. Chem.* **2013**, *5*, 1019.
(9) Ma, L.; Zhang, K.; Kloc, C.; Sun, H.; Michel-Beyerle, M. E.; Gurzadyan, G. G. *Phys. Chem. Chem. Phys.* **2012**, *14*, 8307.
(10) Burdett, J. J.; Bardeen, C. J. *J. Am. Chem. Soc.* **2012**, *134*, 8597.
(11) Pensack, R. D.; Tilley, A. J.; Parkin, S. R.; Lee, T. S.; Payne, M. M.; Gao, D.; Jahnke, A. A.; Oblinsky, D. G.; Li, P.-F.; Anthony, J. E.; Seferos, D. S.; Scholes, G. D. *J. Am. Chem. Soc.* **2015**, *137*, 6790.
(12) Margulies, E. A.; Wu, Y.-L.; Gawel, P.; Miller, S. A.; Shoer, L. E.; Schaller, R. D.; Diederich, F.; Wasielewski, M. R. *Angew. Chem., Int. Ed.* **2015**, *54*, 8679.
(13) Wang, C.; Tauber, M. J. *J. Am. Chem. Soc.* **2010**, *132*, 13988.
(14) Dillon, R. J.; Piland, G. B.; Bardeen, C. J. *J. Am. Chem. Soc.* **2013**, *135*, 17278.
(15) Musser, A. J.; Maiuri, M.; Brida, D.; Cerullo, G.; Friend, R. H.; Clark, J. *J. Am. Chem. Soc.* **2015**, *137*, 5130.
(16) Johnson, J. C.; Nozik, A. J.; Michl, J. *J. Am. Chem. Soc.* **2010**, *132*, 16302.
(17) Johnson, J. C.; Akdag, A.; Zamadar, M.; Chen, X.; Schwerin, A. F.; Paci, I.; Smith, M. B.; Havlas, Z.; Miller, J. R.; Ratner, M. A.; Nozik, A. J.; Michl, J. *J. Phys. Chem. B* **2013**, *117*, 4680.
(18) Eaton, S. W.; Shoer, L. E.; Karlen, S. D.; Dyar, S. M.; Margulies, E. A.; Veldkamp, B. S.; Ramanan, C.; Hartzler, D. A.; Savikhin, S.; Marks, T. J.; Wasielewski, M. R. *J. Am. Chem. Soc.* **2013**, *135*, 14701.
(19) Eaton, S. W.; Miller, S. A.; Margulies, E. A.; Shoer, L. E.; Schaller, R. D.; Wasielewski, M. R. *J. Phys. Chem. A* **2015**, *119*, 4151.
(20) Hartnett, P. E.; Margulies, E. A.; Mauck, C. M.; Miller, S. A.; Wu, Y.; Wu, Y.-L.; Marks, T. J.; Wasielewski, M. R. *J. Phys. Chem. B* **2016**, *120*, 1357.
(21) Johnson, J. C.; Nozik, A. J.; Michl, J. *Acc. Chem. Res.* **2013**, *46*, 1290.
(22) Zirzlmeier, J.; Casillas, R.; Reddy, S. R.; Coto, P. B.; Lehnherr, D.; Chernick, E. T.; Papadopoulos, I.; Thoss, M.; Tykwinski, R. R.; Guldi, D. M. *Nanoscale* **2016**, *8*, 10113.
(23) Zirzlmeier, J.; Lehnherr, D.; Coto, P. B.; Chernick, E. T.; Casillas, R.; Basel, B. S.; Thoss, M.; Tykwinski, R. R.; Guldi, D. M. *Proc. Natl. Acad. Sci. U. S. A.* **2015**, *112*, 5325.

(24) Lukman, S.; Musser, A. J.; Chen, K.; Athanasopoulos, S.; Yong, C. K.; Zeng, Z.; Ye, Q.; Chi, C.; Hodgkiss, J. M.; Wu, J.; Friend, R. H.; Greenham, N. C. *Adv. Funct. Mater.* **2015**, *25*, 5452.

(25) Margulies, E. A.; Miller, C. E.; Wu, Y.; Ma, L.; Schatz, G. C.; Young, R. M.; Wasielewski, M. R. *Nat. Chem.* **2016**, *8*, 1120−1125.

(26) Fuemmeler, E. G.; Sanders, S. N.; Pun, A. B.; Kumarasamy, E.; Zeng, T.; Miyata, K.; Steigerwald, M. L.; Zhu, X. Y.; Sfeir, M. Y.; Campos, L. M.; Ananth, N. *ACS Cent. Sci.* **2016**, *2*, 316.

(27) Greyson, E. C.; Vura-Weis, J.; Michl, J.; Ratner, M. A. *J. Phys. Chem. B* **2010**, *114*, 14168.

(28) Scholes, G. D. *J. Phys. Chem. A* **2015**, *119*, 12699.

(29) Monahan, N.; Zhu, X. Y. *Annu. Rev. Phys. Chem.* **2015**, *66*, 601.

(30) Bakulin, A. A.; Morgan, S. E.; Kehoe, T. B.; Wilson, M. W. B.; Chin, A. W.; Zigmantas, D.; Egorova, D.; Rao, A. *Nat. Chem.* **2016**, *8*, 16−23.

(31) Nolde, F.; Qu, J.; Kohl, C.; Pschirer, N. G.; Reuther, E.; Müllen, K. *Chem. - Eur. J.* **2005**, *11*, 3959.

(32) Nakazono, S.; Easwaramoorthi, S.; Kim, D.; Shinokubo, H.; Osuka, A. *Org. Lett.* **2009**, *11*, 5426.

(33) Young, R. M.; Dyar, S. M.; Barnes, J. C.; Juricek, M.; Stoddart, J. F.; Co, D. T.; Wasielewski, M. R. *J. Phys. Chem. A* **2013**, *117*, 12438.

(34) Young, R. M.; Singh, A. P.; Thazhathveetil, A. K.; Cho, V. Y.; Zhang, Y.; Renaud, N.; Grozema, F. C.; Beratan, D. N.; Ratner, M. A.; Schatz, G. C.; et al. *J. Am. Chem. Soc.* **2015**, *137*, 5113.

(35) te Velde, G.; Bickelhaupt, F. M.; Baerends, E. J.; Fonseca Guerra, C.; van Gisbergen, S. J. A.; Snijders, J. G.; Ziegler, T. *J. Comput. Chem.* **2001**, *22*, 931.

(36) Berkelbach, T. C.; Hybertsen, M. S.; Reichman, D. R. *J. Chem. Phys.* **2013**, *138*, 114103.

(37) Klebe, G.; Graser, F.; Hadicke, E.; Berndt, J. *Acta Crystallogr., Sect. B: Struct. Sci.* **1989**, *45*, 69.

(38) Holtrup, F. O.; Müller, G. R. J.; Quante, H.; De Feyter, S.; De Schryver, F. C.; Müllen, K. *Chem. - Eur. J.* **1997**, *3*, 219.

(39) Würthner, F.; Saha-Moeller, C. R.; Fimmel, B.; Ogi, S.; Leowanawat, P.; Schmidt, D. *Chem. Rev.* **2016**, *116*, 962.

(40) Sung, J.; Nowak-Krol, A.; Schlosser, F.; Fimmel, B.; Kim, W.; Kim, D.; Würthner, F. *J. Am. Chem. Soc.* **2016**, *138*, 9029.

(41) Spano, F. C. *Acc. Chem. Res.* **2010**, *43*, 429.

(42) Kistler, K. A.; Pochas, C. M.; Yamagata, H.; Matsika, S.; Spano, F. C. *J. Phys. Chem. B* **2012**, *116*, 77.

(43) Settels, V.; Liu, W.; Pflaum, J.; Fink, R. F.; Engels, B. *J. Comput. Chem.* **2012**, *33*, 1544.

(44) Kasha, M.; Rawls, H. R.; El-Bayoumi, M. A. *Pure Appl. Chem.* **1965**, *11*, 371.

(45) Rao, A.; Wilson, M. W. B.; Albert-Seifried, S.; Di Pietro, R.; Friend, R. H. *Phys. Rev. B: Condens. Matter Mater. Phys.* **2011**, *84*, 195411.

(46) Wong, W. K.; Westrum, E. F. *Mol. Cryst. Liq. Cryst.* **1980**, *61*, 207.

(47) Lee, S. K.; Zu, Y.; Herrmann, A.; Geerts, Y.; Müllen, K.; Bard, A. J. *J. Am. Chem. Soc.* **1999**, *121*, 3513.

(48) Margulies, E. A.; Shoer, L. E.; Eaton, S. W.; Wasielewski, M. R. *Phys. Chem. Chem. Phys.* **2014**, *16*, 23735.

(49) Carmichael, I.; Hug, G. L. *J. Phys. Chem. Ref. Data* **1986**, *15*, 1.

(50) Sanders, S. N.; Kumarasamy, E.; Pun, A. B.; Trinh, M. T.; Choi, B.; Xia, J.; Taffet, E. J.; Low, J. Z.; Miller, J. R.; Roy, X.; Zhu, X. Y.; Steigerwald, M. L.; Sfeir, M. Y.; Campos, L. M. *J. Am. Chem. Soc.* **2015**, *137*, 8965.

(51) Greyson, E. C.; Stepp, B. R.; Chen, X.; Schwerin, A. F.; Paci, I.; Smith, M. B.; Akdag, A.; Johnson, J. C.; Nozik, A. J.; Michl, J.; Ratner, M. A. *J. Phys. Chem. B* **2010**, *114*, 14223.

(52) Renaud, N.; Sherratt, P. A.; Ratner, M. A. *J. Phys. Chem. Lett.* **2013**, *4*, 1065.

(53) Smith, M. B.; Michl, J. *Annu. Rev. Phys. Chem.* **2013**, *64*, 361.